Contents lists available at ScienceDirect

Acta Biomaterialia

3D printed Ti6Al4V implant surface promotes bone maturation and retains a higher density of less aged osteocytes at the bone-implant interface

Furqan A. Shah [a,b,*], Anders Snis [c], Aleksandar Matic [d], Peter Thomsen [a,b], Anders Palmquist [a,b]

[a] Department of Biomaterials, Institute of Clinical Sciences, Sahlgrenska Academy at University of Gothenburg, Göteborg, Sweden
[b] BIOMATCELL VINN Excellence Center of Biomaterials and Cell Therapy, Göteborg, Sweden
[c] Arcam AB, Mölndal, Sweden
[d] Department of Applied Physics, Chalmers University of Technology, Göteborg, Sweden

ARTICLE INFO

ABSTRACT

For load-bearing orthopaedic applications, metal implants having an interconnected pore structure exhibit the potential to facilitate bone ingrowth and the possibility for reducing the stiffness mismatch between the implant and bone, thus eliminating stress-shielding effects. 3D printed solid and macroporous Ti6Al4V implants were evaluated after six-months healing in adult sheep femora. The ultrastructural composition of the bone-implant interface was investigated using Raman spectroscopy and electron microscopy, in a correlative manner. The mineral crystallinity and the mineral-to-matrix ratios of the interfacial tissue and the native bone were found to be similar. However, lower Ca/P ratios, lower carbonate content, but higher proline, phenylalanine and tyrosine levels indicated that the interfacial tissue remained less mature. Bone healing was more advanced at the porous implant surface (vs. the solid implant surface) based on the interfacial tissue ν_1 CO_3^{2-}/ν_2 PO_4^{3-} ratio, phenylalanine and tyrosine levels approaching those of the native bone. The mechanosensing infrastructure in bone, the osteocyte lacuno-canalicular network, retained ~40% more canaliculi per osteocyte lacuna, i.e., a 'less aged' morphology at the interface. The osteocyte density per mineralised surface area was ~36–71% higher at the interface after extended healing periods.

Statement of significance

In osseointegration research, the success of an implant surface or design is commonly determined by quantifying the amount of new bone, rather than its maturation, composition and structure. This work describes a novel correlative methodology to investigate the ultrastructure and composition of bone formed around and within 3D printed Ti6Al4V implants having an interconnected open-pore structure. Raman spectroscopy demonstrates that the molecular composition of the interfacial tissue at different implant surfaces may vary, suggesting differences in the extent to which bone maturation occurs even after long-term healing. Bone maturation corresponded well with the structural parameters associated with remodelling kinetics, for example, the osteocyte density and the average number of canaliculi per osteocyte lacuna.

1. Introduction

For orthopaedic applications, porous metal implants having an interconnected pore structure are of particular interest due to their potential ability to facilitate tissue ingrowth and therefore present the possibility for reducing the stiffness mismatch between the load-bearing metal implant and bone, thus eliminating stress-shielding effects [1]. With the use of electron beam melting (EBM) processing technique, the elastic modulus of porous Ti6Al4V can be tailored to be similar to that of bone, thus minimising the stress-shielding effect [2]. The native EBM surface allows bone ingrowth into the surface irregularities, with bone-implant contact levels at par with machined surfaces prepared by wrought and EBM techniques [3]. Moreover, implants with an interconnected

* Corresponding author at: Department of Biomaterials, Sahlgrenska Academy at University of Gothenburg, Göteborg, Sweden.
E-mail address: furqan.ali.shah@biomaterials.gu.se (F.A. Shah).

pore structure support bone formation not only around the implant but also deep within the porous network, with high levels of bone-implant contact and bone volume [4].

Osteoblasts (Ob), the bone-forming cells, destined to become osteocytes (Ot) slow down matrix production and become entrapped as their neighbouring osteoblasts continue to produce matrix actively [8]. The long dendritic processes of osteocytes sense mechanical loading, which is believed to be essential for bone remodelling [9]. Presumably, osteocytes are involved in biomineralisation and the phosphate metabolism [10]. Structurally, the osteocyte lacuno-canalicular network organisation reflects the extracellular matrix orientation – the osteocytes are aligned parallel to the lamellar direction while the canaliculi extend perpendicularly [11]. Moreover, the osteocyte morphology shows age-related changes, and an inverse relationship has been described between the average number of osteocyte canaliculi per osteocyte lacuna (N.Ot.Ca/Ot.Lc) and tissue age [12]. Furthermore, the osteocyte number influences bone remodelling [13] and age-related decrease in the osteocyte density may cause deteriorations in canalicular fluid flow and reduce the detection of microdamage, which compromises the structural integrity and contributes to bone fragility [14].

Bone exhibits a hierarchical architecture [5] composed of an organic matrix phase dominated by type-I collagen and the inorganic mineral phase, ion-substituted apatite [6]. The relative mineral content and the degree of carbonate substitution are often believed to be the strongest predictors of mechanical properties and are often correlated with the crystallinity of the mineral phase, which in turn is related to the elastic modulus, yield stress, and fracture stress [7]. With advancing tissue age, increase in the degree of mineralisation [15] and concurrently declining collagen content, and changes in inter- and intrafibrillar crosslinking [16] contribute towards decreases in the ductility and fracture toughness of bone. The substitution of CO_3^{2-} ions for OH^- and PO_4^{3-} ions creates vacancies and distortions that may change the shape of the apatite crystal lattice, resulting in alterations in the local strain environment, consequently affecting the mechanical strength of a mineral crystal [17]. While bone apatite does not contain a high concentration of hydroxyl (OH^-) groups [18], 40–50% of the OH^- groups are not substituted [19], and the amount of apatite hydroxylation is related to the degree of atomic ordering [20].

In order to understand the mechanisms underlying bone strength, Raman spectroscopy has been used extensively to characterise the organic and inorganic components of bone [21]. While X-ray diffraction probes the ordering of atomic planes, Raman scattering is sensitive to atomic scale distortion, i.e., on the unit cell level [18]. In synthetic carbonated apatites, increased mineral crystallinity results in sharpening of the main phosphate band (ν_1 PO_4^{3-}) at 959 cm^{-1} which is reflected in reduced carbonate content, i.e., decreased carbonate-to-phosphate ratio [22]. In contrast, the mineral crystallinity in bone may remain unchanged despite an observed increase in carbonate-to-phosphate ratios [23]. It is, however, important to recognise that relative to the organic component, the phosphate content (not the ratio of phosphate-to-carbonate) determines the mechanical properties of bone [17]. The high carbonate content of bone apatite constrains the dimensions of apatite crystallites to the nanometre scale, which in turn controls the internal structure of the mineral crystallite [18].

Previous investigations on osseointegration using Raman spectroscopy [24–27] have focused on the detection of the 959–964 cm^{-1} phosphate band, with little consideration of other parameters influencing bone quality, e.g., crystallinity of the mineral phase, carbonate substitution, the relative amounts of the inorganic and the organic phases, and the composition of the organic matrix containing collagen and other non-collagenous proteins. On Raman spectra, the Amide (I and III) bands represent peptide bonds within proteins. In collagen, they indicate the formation of interchain hydrogen bonds (i.e., between the N–H groups of glycines and the C=O groups of prolines in neighbouring chains), and therefore represent stabilisation of the structure on the subfibrillar level [28].

The present work investigates bone formed adjacent to 3D printed macro-porous and solid Ti6Al4V implants fabricated by the EBM technique, with the aim to answer three key questions: (i) How does the ultrastructural composition of the interfacial tissue differ from the native bone after prolonged healing? (ii) Does implant surface structure affect interfacial bone composition? and (iii) Does bone form differently inside the open-pore area compared to the outside?

2. Materials and methods

2.1. Implant fabrication, animal surgery, and sample processing

Two types of implants, (i) solid and (ii) porous, all 7 mm in length and 5.2 mm in diameter, were manufactured from a standard Arcam Ti6Al4V extra low interstitial (ELI) powder (particle size of 45–100 μm) as the starting material in an Arcam EBM S12 system [4]. The layer thickness of the build process was 70 μm. All implants were manufactured in the same build cycle at an average build temperature of 680 °C and 0.2 Pa vacuum pressure. The build was cooled down to 100 °C in a helium atmosphere of 2×10^4 Pa before being taken out. All implants were blasted with the Ti6Al4V ELI powder. Solid implants were obtained by machining cylindrical rods obtained from the same build cycle. The porous implants retained the EBM surface, with the lower 2/3rd being an open-pore area with a network of interconnected struts. The animal surgery has been described in detail previously [4], and the study was conducted in accordance with the FDA Good Laboratory Practice (GLP) regulations. Briefly, three sheep were anaesthetised by intravenous administration of a mixture of thiopental (Nesdonal®, Merial, France), pentobarbital (sodium pentobarbital, CEVA Santé animale, France), and atropine (Atropinum sulfuricum, Aguettant, France), followed by inhalation of an O_2-isoflurane (Aeranne®, Baxter, 1–4%) mixture. Penicillin-procaine and penicillin-benzathine (Duplocilline®, Intervet, France) were administered immediately preoperatively, and at 3rd, 6th, and 9th days postoperatively. Analgesia was administered preoperatively (flunixine, Meflosyl® Injectable, Fort Dodge, France; and buprenorphine hydrochloride, Temgesic®, Schering-Plough) and postoperatively every 2 days for one week. The distal femoral epiphyses were exposed; implant holes were sequentially enlarged using water-cooled 2, 4.3, and 5 mm diameter orthopaedic drills and two implants were installed in each leg by press fitting. The animals were euthanised 26 weeks after surgery by barbiturate overdose (DolethalND, Vetoquinol). The implants with surrounding bone were harvested, immersion fixed in 10% neutral buffered formalin, and dehydrated in a graded ethanol series prior to embedding in LR White resin (London Resin Company, UK). The embedded blocks were bisected longitudinally (EXAKT® Apparatebau GmbH & Co, Norderstedt, Germany) [29]. For the purpose of the present ultrastructural investigation, three implants of each type, i.e., one implant of either type from each animal, were used.

2.2. Characterisation of the surface structure

To analyse the surface structure of the implants, X-ray micro-computed tomography (Skyscan 1172, Bruker micro-CT, Kontich, Belgium) was performed at 100 kV energy with an Al/Cu filter, for a complete 360° rotation at a step size of 0.7° with an averaging of 5 frames and an image pixel size of 11.88 μm. Reconstructed

transaxial images were obtained in the NRecon software (Bruker micro-CT, Kontich, Belgium) resulting in a 3D stack of 635 slices. Visualisation and 3D analysis were performed using associated PC programs (Image viewer, CTVox, and CTAn).

The implant surfaces were also examined by secondary electron scanning electron microscopy (SE-SEM, Ultra 55 FEG SEM, Leo Electron Microscopy Ltd, UK) operated at 5 kV accelerating voltage, 10 mm working distance and 30 μm aperture size.

2.3. Microstructural analysis

Bone formation around the implants and bone ingrowth into the open-pore area of the porous implants was qualitatively investigated in 3D by X-ray micro-CT (Skyscan 1172, Bruker, Kontich, Belgium), and visualisation was performed in CTVox. The bone-implant interface was evaluated by backscattered electron scanning electron microscopy (BSE-SEM, FEI Quanta 200 FEG ESEM) performed without an electrically conductive coating, at 0.5 Torr water-vapour pressure (low vacuum), 20 kV accelerating voltage and 10 mm working distance.

2.4. Spectroscopic analysis

Raman spectroscopy was used to investigate the composition of the interfacial tissue and the native bone. Spectra were collected at room temperature by a nitrogen cooled charge-coupled device (CCD) detector connected to a Dilor XY 800 spectrometer (Horiba, Jobin Yvon GmbH), equipped with a 676 nm Ar/Kr laser operated at ~20 mW, with a 100× objective, 600 groove/mm grating, 300 mm focal length and pinhole size of 530 μm. One sample-pair (from the same animal) was used. Six different locations along the implant surface, selected by prior BSE-SEM imaging, were analysed for each group, 5–10 μm from the implant surface; three at the upper 1/3rd and three at the lower 2/3rd regions, the latter being within the open-pore area for the porous implants. Areas where bone remodelling was still going on were avoided. For the native bone, six locations were analysed along the trabecular midline, $\geqslant 1.5$ mm from the implant surface. A reference spectrum for the embedding resin was also recorded (provided as supplementary data). At least three acquisitions were made at each location with an integration time of 300 s each. Raw spectra were truncated between 300–1800 cm^{-1} and background fluorescence subtraction was performed by fitting a sixth order polynomial function using the Background Correction program [30] for MATLAB R2013b (Mathworks Inc., Natick, MA). The wavenumber axis was adjusted so that the ν_1 PO$_4^{3-}$ peaks in all spectra corresponded to ~959 cm^{-1}. The baseline-corrected spectra were then normalised to the intensity of the ν_1 PO$_4^{3-}$ band using Plot (http://plot.micw.eu/). Curve fitting, using mixed Gaussian and Lorentzian functions, and quantification of integral areas was done using MagicPlot (www.magicplot.com).

The Raman metrics investigated included mineral crystallinity, taken as the reciprocal of the full-width at half-maximum (1/FWHM) of the ν_1 PO$_4^{3-}$ peak [31], apatite-to-collagen ratio, also referred to as the mineral-to-matrix ratio (ν_2 PO$_4^{3-}$/Amide III [32,33]; ν_1 PO$_4^{3-}$/Amide I [34]), the carbonate-to-phosphate ratio (ν_1 CO$_3^{2-}$/ν_1 PO$_4^{3-}$ [35]; ν_1 CO$_3^{2-}$/ν_2 PO$_4^{3-}$ [36]), the carbonate-to-matrix (ν_1 CO$_3^{2-}$/Amide I [37,38]) ratio, and the Amide I/Amide III ratios [39]. The relative amounts of amino acids proline (Pro/ν_1 PO$_4^{3-}$), phenylalanine (Phe/ν_1 PO$_4^{3-}$), and tyrosine (Tyr/ν_1 PO$_4^{3-}$) in relation to the main phosphate peak at 959 cm^{-1}, phenylalanine-to-tyrosine (Phe/Tyr) ratios, and phenylalanine-to-carbonate (Phe/ν_1 CO$_3^{2-}$) ratios were also investigated to understand the composition of the organic phase of the bone interfacing the implant surface (Table 1). The integral areas were: ν_1 PO$_4^{3-}$ (~930–980 cm^{-1}), ν_2 PO$_4^{3-}$ (~410–460 cm^{-1}), Amide I (~1620–1700 cm^{-1}), Amide III (~1215–1300 cm^{-1}), and ν_1 CO$_3^{2-}$ (~1050–1100 cm^{-1}) [34].

Energy dispersive X-ray spectroscopy (INCA EDX system, Oxford Instruments GmbH, Wiesbaden, Germany) was performed at 20 kV accelerating voltage, 10 mm working distance, 120 μm aperture size, 60 s live-time, and 0–10 keV spectral energy range, to evaluate the elemental composition of the interfacial tissue within 20 μm from the implant surface, as well as the native bone. One sample-pair (from the same animal) was used. Six different locations along the implant surface were analysed for each group; three at the upper 1/3rd and three at the lower 2/3rd regions, the latter being within the open-pore area for the porous implants. During sample preparation, a 1–2 μm gap had appeared at the interface, separating the bone from the implant surface. Avoiding this separation artefact, five evenly spaced spectra were recorded between 2 and 17 μm from the tissue edge. For the native bone, five evenly spaced spectra were also recorded at six different locations along the trabecular midline, $\geqslant 1.5$ mm from the implant surface. The mean values of the five individual spectra recorded at each location were used for statistical analysis.

2.5. Direct visualisation of osteocyte morphology

Resin embedded bone-implant blocks were prepared for direct visualisation of osteocytes adjacent to the implant surface, as well as in areas of native bone distant from the implant, using a resin cast etching procedure [45]. The surface of the resin embedded blocks was wet polished with 400–4000 grit SiC grinding paper. The samples were then immersed in 9% H$_3$PO$_4$ (for 30 s), rinsed in Milli-Q water (for 5 s), immersed in 5% NaOCl (for 5 min), rinsed again (for 30 s) and allowed to air-dry overnight. The samples were Au sputter-coated (~10 nm) for high vacuum SE-SEM imaging (Ultra 55 FEG SEM, Leo Electron Microscopy Ltd, UK) operated at 5 kV accelerating voltage, 5 mm working distance, and 30 μm aperture size.

The number of osteocyte canaliculi per osteocyte lacuna (N.Ot. Ca/Ot.Lc) was quantified on images recorded at ×5000–10,000 magnifications. At the interfacial region, only the first and the second osteocyte layers from the implant surface were considered, while for the native bone, osteocytes located along the trabecular midline and furthest from either trabecular surface, $\geqslant 1.5$ mm from the implant surface, were recorded.

The osteocyte density, i.e., the average number of osteocytes per mineralised surface area (N.Ot/B.Ar), was quantified on images recorded at ×200 magnification. For the N.Ot/B.Ar at the interface, osteocytes (in the new bone) located up to 300 μm from the

Table 1
Raman spectroscopic band assignments for bone mineral and matrix components.

Raman shift (cm^{-1})	Assignment	Comments/Reference
430	ν_2 PO$_4^{3-}$	
579	ν_4 PO$_4^{3-}$	
853	Proline (Pro)	ν(C–C)
872	Hydroxyproline (Hyp)	ν(C–C)
920	Proline (Pro)	[40]
959	ν_1 PO$_4^{3-}$	Strongest marker for bone mineral
1003	Phenylalanine (Phe)	ν(C–C)
1070–72	ν_1 CO$_3^{2-}$; B-type	
1103	ν_1 CO$_3^{2-}$; A-type	[41]
1240; 1270	Amide III	ν(C–N); δ(N–H); collagen type-I
1446	δ(CH$_3$), δ(CH$_2$)	Collagen, non-collagenous proteins [42], PMMA [32]
1604–1607	Tyrosine	δ(C=C) [43,44]
1660; 1690	Amide I	ν(C=O); collagen type-I

implant surface were considered. To account for topological differences, the 300 μm limit in the upper 1/3rd (~1.4 mm wide area) of the porous implant was delineated by a line following the micro-contour of the implant surface. In the lower 2/3rd (open-pore region), only the osteocytes that were within the confines of the implant were considered. For the native bone, images were recorded ⩾1.5 mm from the implant surface. All unmineralised areas in each recorded image were excluded by segmentation using ImageJ (imagej.nig.gov/ij) and the osteocytes were quantified using the Cell Counter plugin.

2.6. Statistical analysis

The Kruskal–Wallis test followed by the Mann–Whitney U test were used for all statistical analyses between the interfacial tissue and the native bone, and between the implant types (SPSS Statistics, v.22, IBM Corporation); p values < 0.05 were considered statistically significant. Mean values ± standard deviations are presented.

3. Results

3.1. Characterisation of the surface structure

The machined surface of the solid implants and the EBM surface of the porous implants exhibited surface areas of 1.098 mm^2 and 1.276 mm^2, respectively, per unit surface area (mm^2) of a theoretically smooth surface. The EBM surface therefore shows a 16.3% enlargement compared to the machined surface due to the surface

irregularities originating from the EBM process (Fig. 1a and b). As the Ti6Al4V ELI powder is prepared by atomisation, the powder particles and therefore surfaces of EBM constructs do not exhibit a high degree of sub-micron scale roughness (Fig. 1c and d).

The interconnected open-pore area of the porous implants comprised of 583 ± 243 μm thick struts (Fig. 1e) with 656 ± 291 μm separations (Fig. 1f) in between. The volume of the open-pore area was approximately 97.8 mm^3 of which the total strut volume was 36.4 mm^3, resulting in an average porosity of 62.7%. The total surface area of the interconnected struts was 249.1 mm^2, i.e., a surface area/volume ratio of 6.84 mm^{-1}.

### 3.2. Microstructural observations

X-ray micro-CT reconstructions showed high levels of bone around the solid and the porous implants and bone ingrowth into the interconnected open-pore area of the porous implants (Fig. S1). BSE-SEM confirmed highly mineralised bone around both the solid and the porous implants (Fig. 2). Bone ingrowth had also occurred into the open-pore area in the lower 2/3rd region of the porous implants. The lamellar pattern closely followed the surface contour, indicating that bone formation began at the implant surface and was directed progressively outward.

3.3. Spectroscopic analysis

For both the solid and porous implants, the Raman spectra recorded from the upper 1/3rd and the lower 2/3rd areas appeared
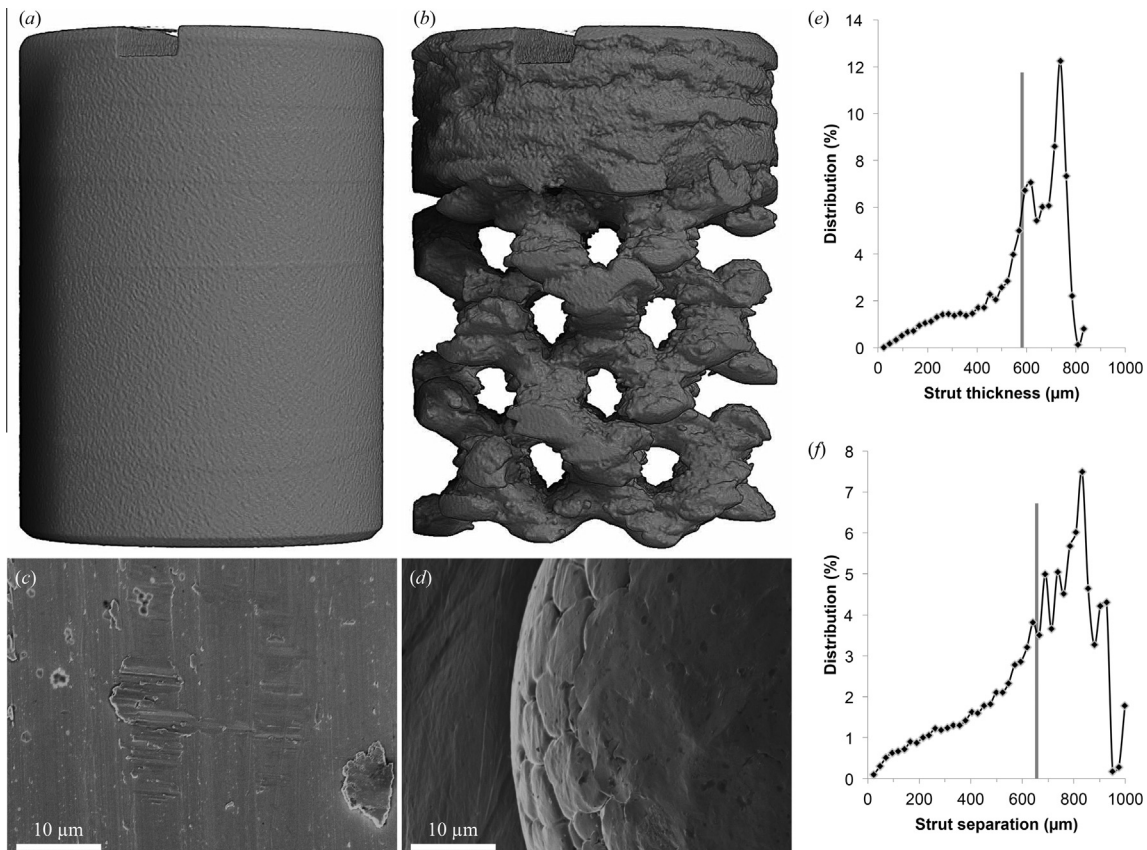
Fig. 1. X-ray micro-computed tomography reconstructions of the (a) solid implants with the machined surface, and the (b) porous implants with the electron beam melted (EBM) surface. SE-SEM images of the (c) machined surface of the solid implants, and the (d) EBM surface of the porous implants. Quantitative X-ray micro-CT analysis from within the interconnected open-pore region (lower 2/3rd) of the porous implants showing the distributions of (e) strut thickness and (f) strut separation. The vertical lines indicate mean values.
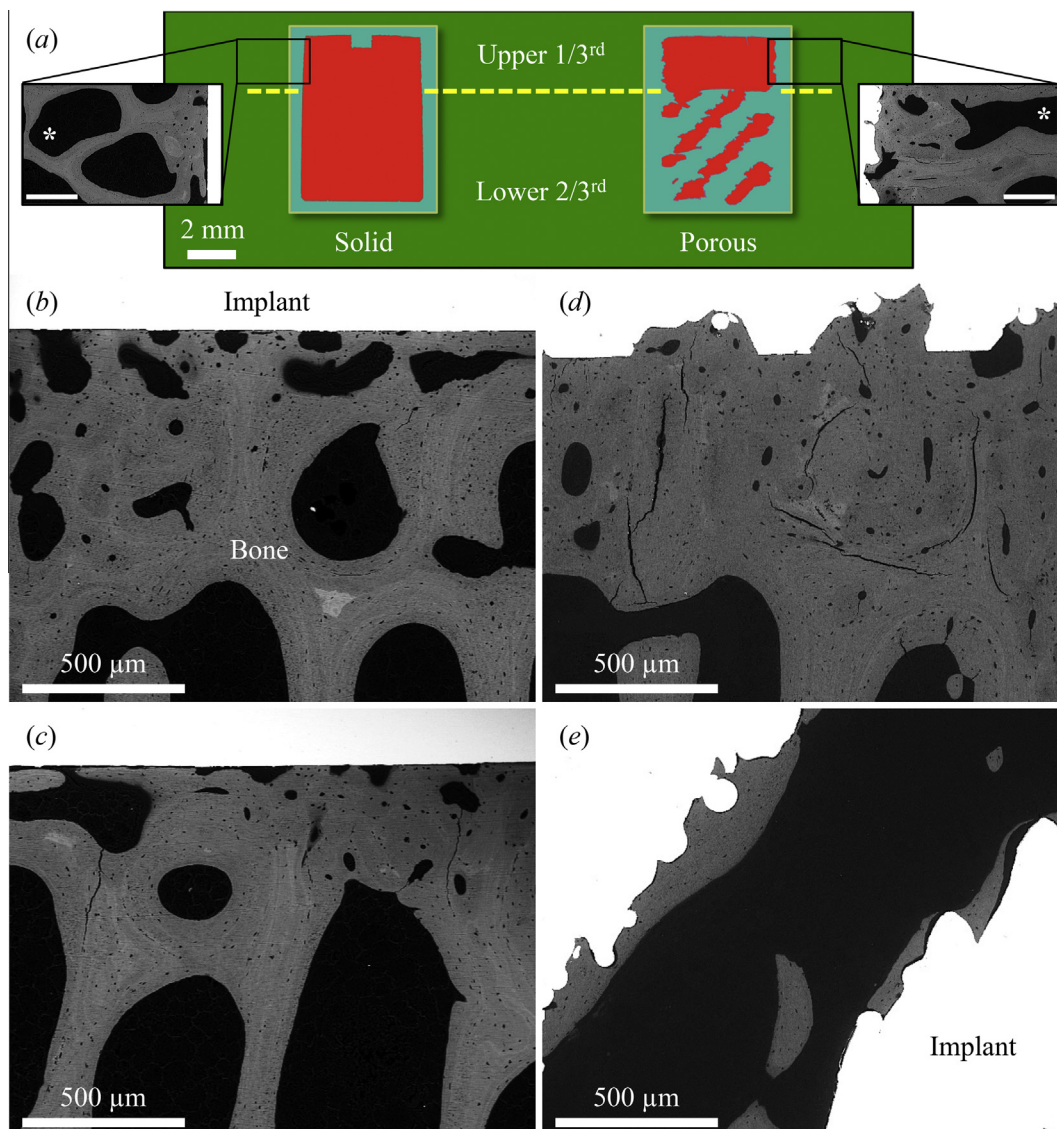
Fig. 2. (a) Schematic illustrating the designation of the upper 1/3rd and lower 2/3rd regions (Nikon SMZ1500 stereomicroscope equipped with an HR Plan Apo 1X objective lens). BSE-SEM images demonstrate the continuity between the interfacial tissue and the native bone (scale bars = 500 μm). All analyses of the native bone were performed at a minimum distance of 1.5 mm from the implant surface (asterisks). BSE-SEM images from (b) the upper 1/3rd region, and (c) the lower 2/3rd region of the solid implants. BSE-SEM images from (d) the upper 1/3rd region, and (e) the lower 2/3rd region of the porous implants.

similar, and therefore the spectra from both locations were pooled for further analysis (Fig. S2).

Relative to the main phosphate vibration at 959 cm^{-1}, several changes could be observed, for example Pro, Phe, v_1 CO_3^{2-}, δ(CH$_3$), δ(CH$_2$), and Tyr (Fig. 3). The most pronounced changes included an approximately proportional increase in the Phe and Tyr signals. For both implant types, the amino acid (proline, phenylalanine, and tyrosine) signals were stronger at the interfacial bone tissue than in the native bone. Despite differences in Phe and Tyr content (Phe and Tyr levels decreased in the order solid implants > porous implants > native bone), a correlation was observed between Phe and Tyr peak intensities (R^2 = 0.94), as the Phe/Tyr ratio was comparable for all the groups and ranged between 2.2 and 2.6 (Fig. 3c). The δ(CH$_3$), δ(CH$_2$) deformation band at 1446 cm^{-1} was also considerably stronger at the interfacial tissue than the native bone. In all cases, the Amide III band appeared to resolve into two components at 1240 and 1270 cm^{-1}, and the Amide I/Amide III ratios remained similar between the native bone and the interfacial tissue.

At both implant surfaces, the mineral crystallinity of the interfacial tissue was similar to that of the native bone. The carbonate-to-phosphate ratio, v_1 CO_3^{2-}/v_1 PO_4^{3-} (relative intensities) and v_1 CO_3^{2-}/v_2 PO_4^{3-} (relative integral areas), of the interfacial tissue at both implant surfaces was lower than the native bone; v_1 CO_3^{2-}/v_2 PO_4^{3-} being relatively higher (p < 0.02) for the porous implant compared to the solid implant. The apatite-to-collagen ratio, v_2 PO_4^{3-}/Amide III and v_1 PO_4^{3-}/Amide I, of the interfacial tissue at both implant surfaces was similar to that of the native bone. The carbonate-to-matrix (v_1 CO_3^{2-}/Amide I) ratio of the interfacial tissue at both implant surfaces was lower than the native bone (Fig. 4, Table T1). Closer examination of specific spectral regions revealed the consistent patterns in compositional differences between the native bone and the interfacial tissue (Fig. S3). Pro, Phe, Tyr, and δ(CH$_3$), δ(CH$_2$) signals were lower in the native bone than the interfacial tissue. Moreover, Phe and Tyr levels of the interfacial tissue were higher for the solid implants compared to the porous implants. In contrast, Amide III signals were comparable between the bone and the interfacial tissue, while the v_1
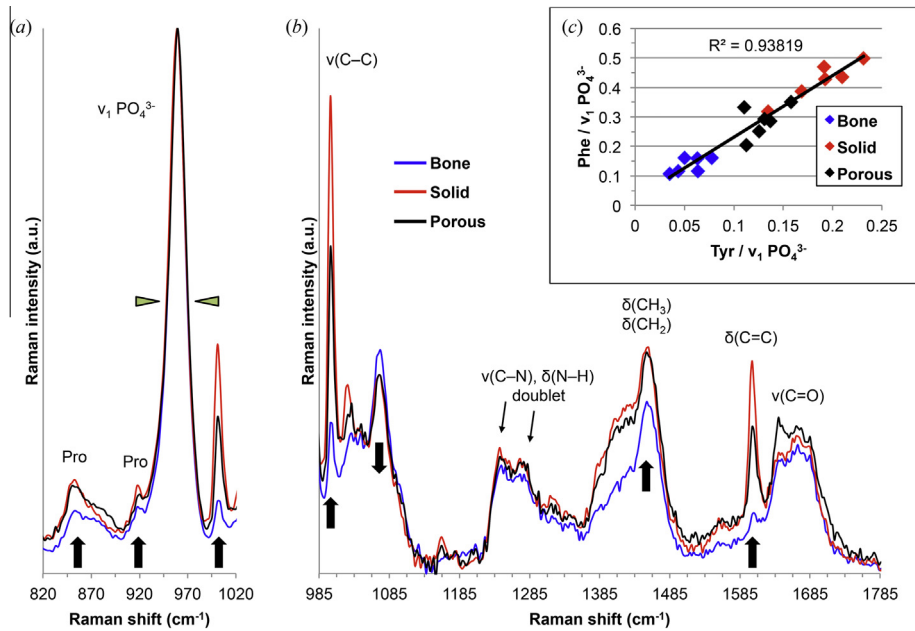
Fig. 3. (a) Spectra normalised to the v_1 PO_4^{3-} peak intensity (average of spectra from six different locations) show similar crystallinity (FWHM indicated by arrowheads) for all the groups, however the interfacial tissue exhibits relatively higher Pro and Phe signals. (b) Compositional differences between the three groups investigated relative to the v_1 PO_4^{3-} peak; the interfacial tissue exhibits higher Phe (1003 cm^{-1}), $\delta(CH_3)$, $\delta(CH_2)$, and Tyr (1604–1607 cm^{-1}) signals, and lower v_1 CO_3^{2-} signals. (c) A positive correlation exists between the relative Phe and Tyr content.
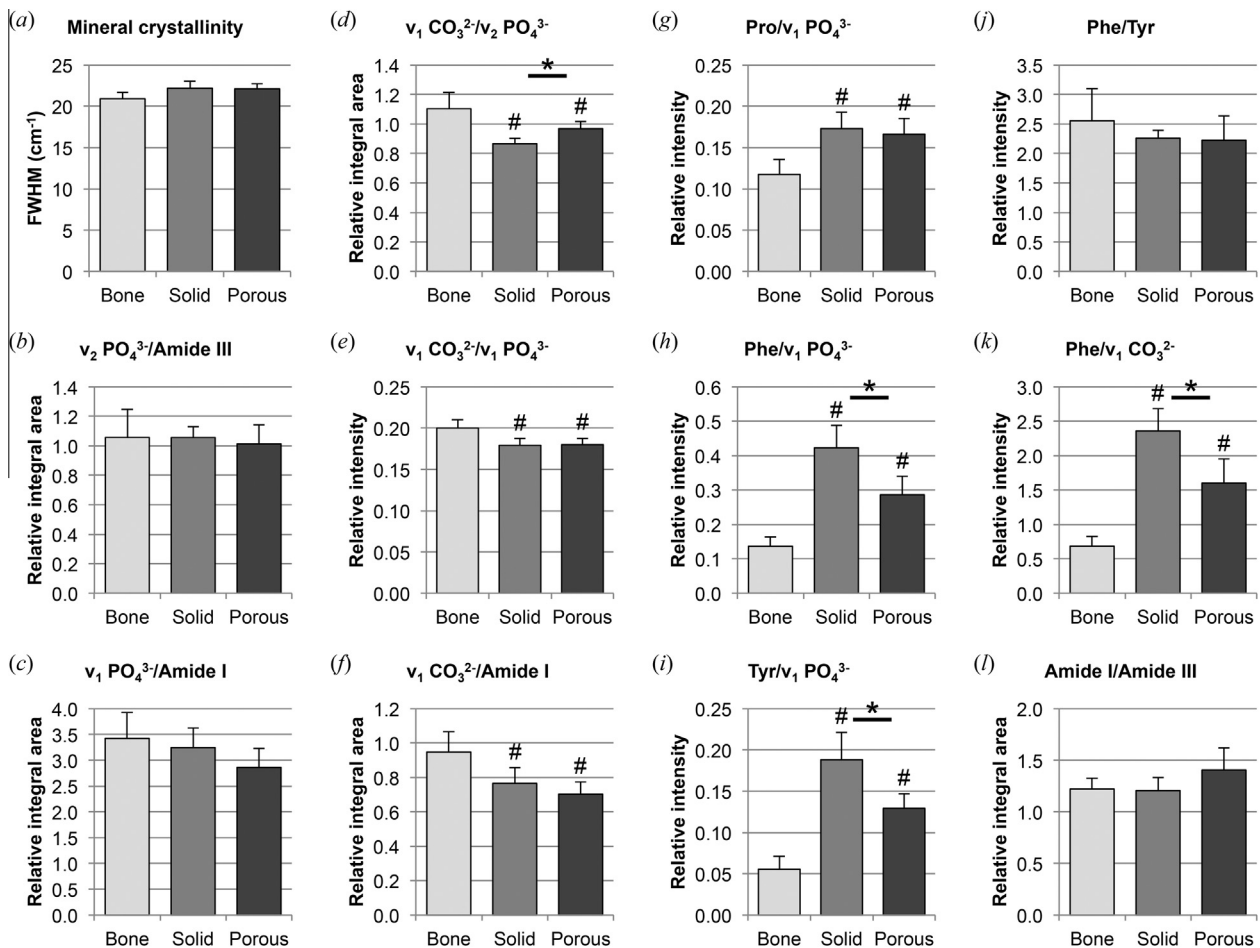
Fig. 4. Raman metrics investigated for the interfacial tissue and native bone (mean values ± SD, # = statistical significance vs. bone, ∗ = statistical significance between the groups indicated by the horizontal bar).
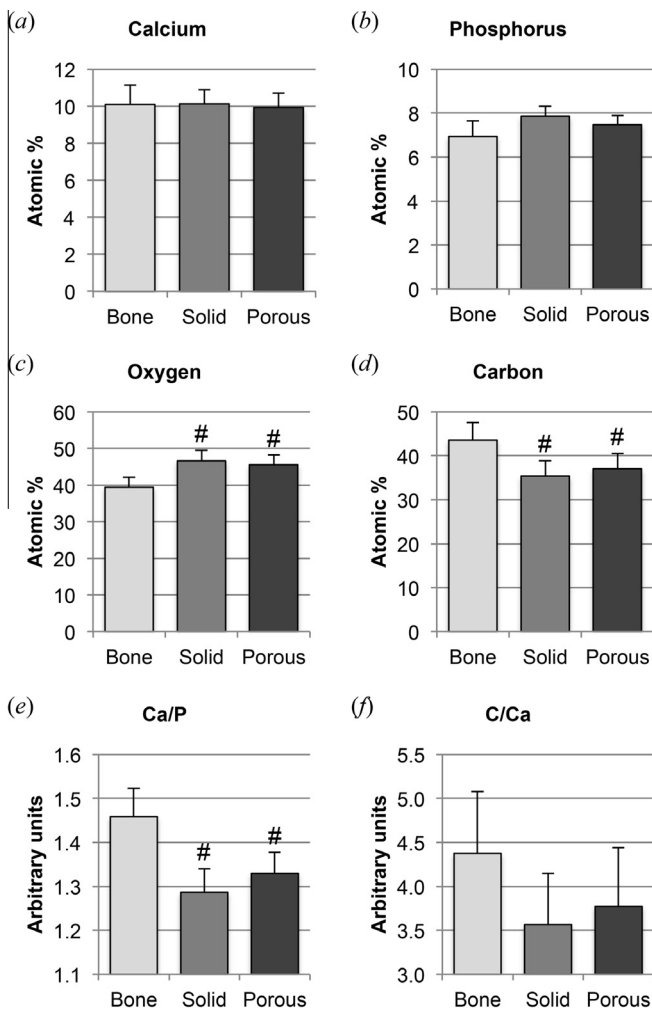
Fig. 5. Elemental analysis by energy dispersive X-ray spectroscopy (EDX) showing the (a) calcium, (b) phosphorus, (c) oxygen, and (d) carbon levels at the interface and in the native bone. (e) Ca/P and (f) C/Ca ratios at the interface and in regions of native bone (mean values ± SD, # = statistical significance vs. bone).

CO_3^{2-} band was consistently higher in all spectra collected from the native bone.

Energy dispersive X-ray spectroscopy revealed calcium, phosphorus, oxygen and carbon as the dominant elements in the native bone. In the interfacial tissue, titanium was also detected in low amounts ($\geqslant 5$ at.%), which may be attributable to the cutting, grinding and polishing procedures, and the large interaction volume of the electron beam. The data was therefore normalised to exclude titanium and other trace elements. For both the solid and porous implants, the Ca/P and C/Ca ratios of the upper 1/3rd and the lower 2/3rd areas were comparable, and therefore the data from both locations were pooled for further analysis.

For both implant types, the calcium and phosphorus content of the interfacial tissue remained similar to the native bone (Fig. 5a and b), the oxygen levels were higher ($p < 0.02$), while the carbon content was lower ($p < 0.04$) (Fig. 5c and d). Compared to the native bone, interfacial tissue Ca/P ratio was lower ($p < 0.005$) for both implant types. The C/Ca ratio remained similar to the native bone (Fig. 5e and f). No other differences in the elemental composition of the interfacial tissue were statistically significant between the solid and porous implants.

3.4. Direct visualisation of osteocyte morphology

Osteocytes at the interface were aligned parallel to the implant surface (Fig. 6) where they appeared to make intimate contact with the implant surface through numerous canaliculi (Fig. 6d–f). In close association with osteocytes and the implant surface, the presence of microvasculature was observed in the bone formed within the open-pore area of the porous implants (Fig. 6g). Osteocytes were also observed within 15–20 μm wide crevices at the junction of the upper 1/3rd and the lower 2/3rd parts of the porous implants (Fig. 6j).

The average number of osteocyte canaliculi per osteocyte lacuna (N.Ot.Ca/Ot.Lc) at the implant interfaces was similar ($p > 0.6$) and 38–42% higher than the native bone ($p < 0.001$ for both implant types) (Fig. 7a–d). Qualitatively, at the porous implants, the N.Ot.Ca/Ot.Lc within the open-pore area (lower 2/3rd) appeared to be indistinguishable from the N.Ot.Ca/Ot.Lc outside (upper 1/3rd). Similarly, the N.Ot.Ca/Ot.Lc at the solid implant surface did not appear to differ between the upper 1/3rd and the lower 2/3rd regions.

In comparison to the native bone, the osteocyte density (N.Ot/B. Ar) was higher at the interface ($p < 0.001$) for both implant surfaces, in both the upper 1/3rd and the lower 2/3rd regions (Fig. 7e). The highest N.Ot/B.Ar increase was observed at the upper 1/3rd of the porous implants (71.2%) (Fig. S4a and b), followed by the lower 2/3rd of the porous implants (44.4%), the upper 1/3rd of the solid implants (38.2%) (Fig. S4c and d) and the lower 2/3rd of the solid implants (35.6%). Overall, the N.Ot/B.Ar was higher ($p < 0.005$) at the porous implant surface than the solid implant surface. The N.Ot/B.Ar in the upper 1/3rd of the porous implants was higher ($p < 0.01$) than the lower 2/3rd (open-pore region) of the porous implants. The N.Ot/B.Ar in the upper 1/3rd of the porous implants was higher ($p < 0.005$) than the upper 1/3rd of the solid implants. The N.Ot/B.Ar in the upper 1/3rd and the lower 2/3rd of the solid implant were comparable ($p > 0.5$). The N.Ot/B.Ar was also similar in the lower 2/3rd ($p > 0.1$) for the two types of implants (Table 2).

4. Discussion

Using implants of distinctly different geometry and surface topography, the composition and ultrastructure of the bone-implant interface was investigated in relation to fully mature native bone. Previous histomorphometric evaluation showed similar amounts of bone-implant contact (60–65%) and bone area (80–90%) up to a distance of 400 μm from both implant designs [4]. In the present work, Raman spectroscopy and direct visualisation of osteocyte morphology by scanning electron microscopy were employed in order to evaluate whether implants with sharply contrasting surface structure are able to induce detectable compositional differences in the interfacial tissue despite there being similarities in the bone morphometric parameters (bone-implant contact and bone area) and structure, on the histological level [3,4].

Generally, with advancing tissue age, the Raman intensity of the $v_1 \, PO_4^{3-}$ peak increases relative to the organic matrix components [31,46], or alternatively the FWHM of the $v_1 \, PO_4^{3-}$ band decreases [47]. Also with tissue age, the intensity of $v_1 \, CO_3^{2-}$ band at 1070 cm^{-1} increases relative to the $v_1 \, PO_4^{3-}$ band [31,46]. These trends are therefore commonly interpreted as markers of bone maturity. Data suggests that the interfacial tissue contains lower carbonate content (relative to phosphate) and higher amino acid content than the native bone. The presence of carbonate in apatite lowers the crystallinity and changes the morphology – crystallites appear more equiaxed rather than needle-like [48]. Due to the
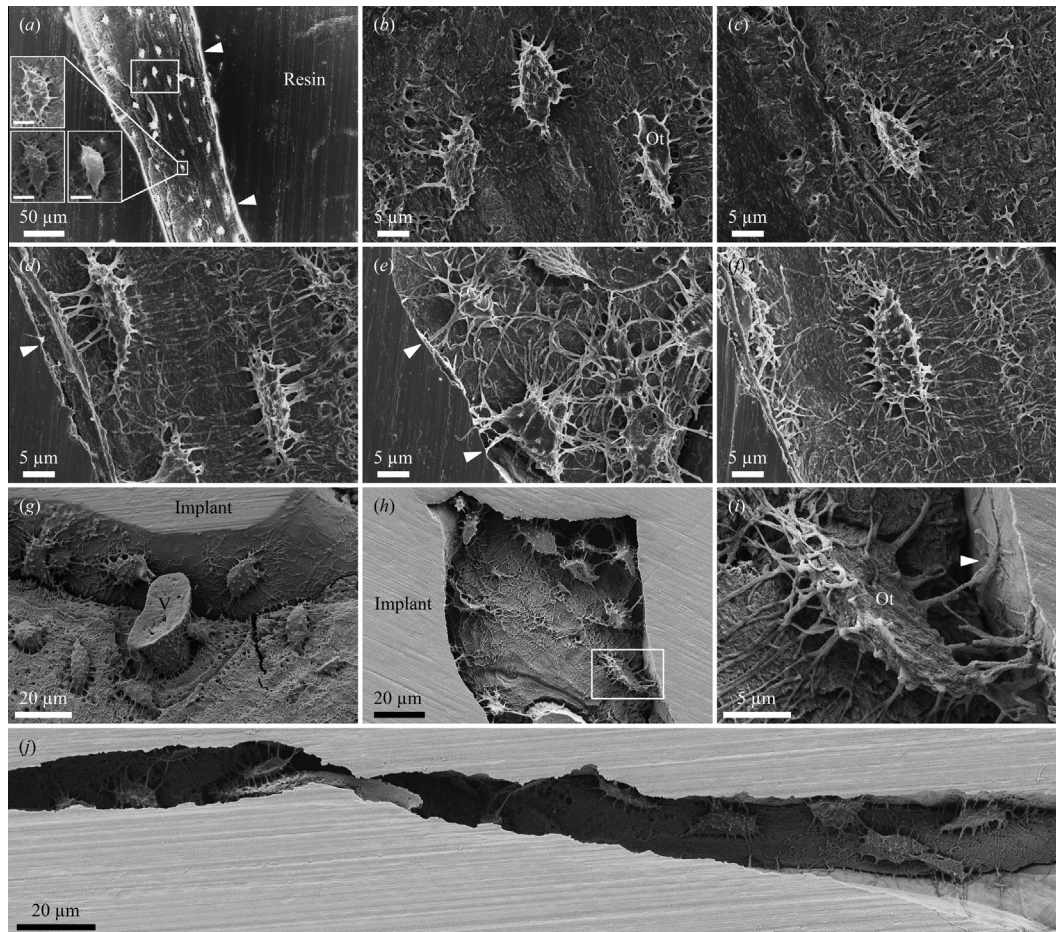
Fig. 6. Direct visualisation of osteocytes (Ot) following resin cast etching. (a) Low-resolution SEM image of a single bone trabecula. Inset images depict the appearance of osteocytes in different imaging modes; top: in-lens detector at 5 kV, bottom-left: secondary electron detector at 5 kV, and bottom-right: secondary electron detector at 20 kV (scale bars = 5 µm). Arrowheads point towards the bone surface. (b) Osteocytes located in the midline (box in a) were considered representative of the 'more aged' phenotype. (c) An osteocyte is aligned parallel to the lamellar direction and the interlamellar seam while the canaliculi extend perpendicularly. (d) The first and second osteocyte layers adjacent to the surface of the implant (arrowhead). (e) Osteocytes adjacent to the implant surface (arrowheads) show a considerably higher number of canaliculi as well as lacuno-canalicular interconnectivity compared to osteocytes located in the trabecular midline (cf. Fig 7b). (f) Qualitatively, interfacial osteocytes appear larger than those in the native bone (compare with c). (g) The resin cast etching technique removed ~25 µm of bone material. Osteocytes maintain close positional association with the vasculature (V) and remain directly attached to the implant surface via a vast canalicular network. Image recorded at 35° stage-tilt. (h) Numerous osteocytes located within an 80 µm wide pore in the implant surface. (i) Higher-resolution image of an osteocyte (box in h) showing direct canalicular attachment and branching onto the implant surface (arrowhead). (j) Numerous osteocytes and an extensive canalicular network within a narrow 15–20 µm wide crevice.

inverse relationship between mineral crystallinity (1/FWHM v_1 PO_4^{3-}) and the degree of carbonation, it is plausible that the lower carbonate content of the interfacial tissue contributes towards the crystallinity of the interfacial tissue and that of the native bone appearing approximately similar. This implies that if the degree of carbonation of the interfacial tissue had been higher, i.e., similar to the native bone, the mineral crystallinity of the interfacial tissue would have been lower. However, despite the comparable mineral crystallinity of the two locations, higher organic content and lower degree of carbonation suggest that the interface zone is relatively less mature, and may be a highly dynamic region in terms of localised remodelling, as pointed out by Steflik et al. by their ultrastructural observation of calcified inclusions and unmineralised areas at the bone-implant interface [49]. Nevertheless, the relative integral area metric, v_1 CO_3^{2-}/v_2 PO_4^{3-}, showed a higher degree of carbonation at the porous implant (vs. the solid implant), suggesting more mature interfacial tissue. The relative intensity ratio metric (v_1 CO_3^{2-}/v_1 PO_4^{3-}), however, remained similar values for both implant types.

The Amide I band is strongly orientation dependent [50]. However, the Amide III band resolved into two component peaks related to the v(C–N) and δ(N–H) deformation modes, respectively

[42], and while their relative intensity ratio may be affected by collagen orientation [51], the δ(N–H) vibration of the N–H groups at ~1240–1246 cm^{-1} in particular, is less sensitive to orientation [28]. The v_2 PO_4^{3-} band is also orientation independent [52]. Therefore, the v_2 PO_4^{3-}/Amide III metric is believed to be the most reliable determinant of the apatite-to-collagen ratio [33]. Despite similar matrix content (v_2 PO_4^{3-}/Amide III), differences were observed in amino acid signals. At the interface, Phe, and Tyr signals were consistently higher at the solid implant interface vs. the porous implant interface, the latter approaching those of the native bone and indicating that bone healing at the porous surface had progressed further than the solid surface. As an index of tissue maturity, older tissue has been demonstrated to have more PO_4^{3-} content in relation to Phe [53]. On the other hand, Tyr is involved in different bone cell metabolic pathways, including the Protein Tyrosine Kinases/Protein Tyrosine Phosphatases (PTKs/PTPs) transduction signalling pathways, which play a role in the control of the osteoblast–osteocyte metabolism. These PTKs/PTPs are involved in the regulation of bone formation [54], and osteoclast remodelling [55].

The δ(CH$_3$), δ(CH$_2$) deformation band at 1446 cm^{-1} indicates the presence of proteins and while it was significantly stronger at the
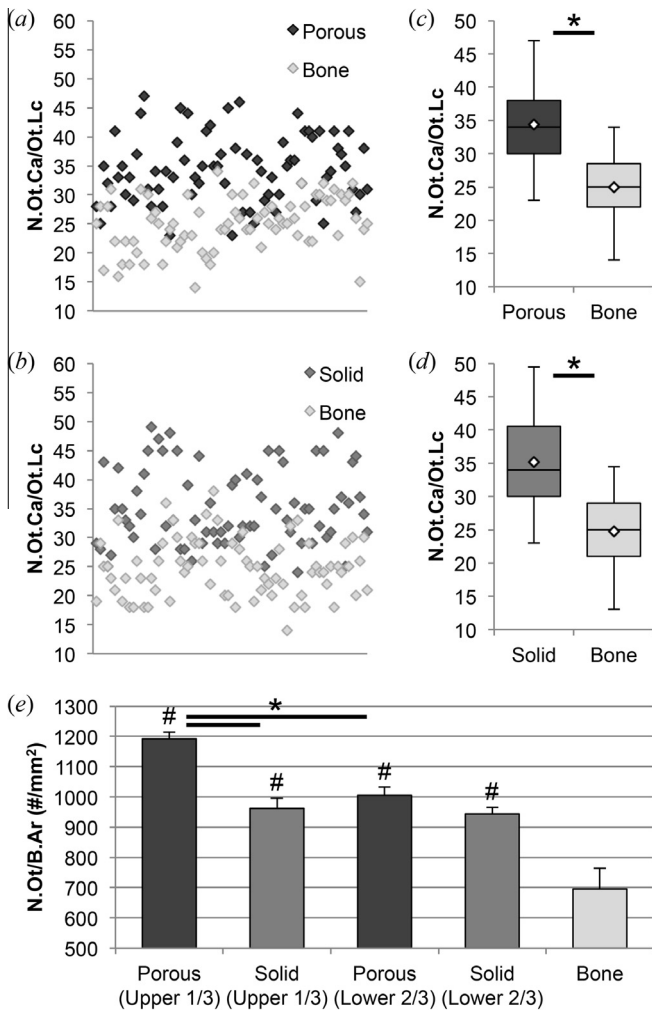
Fig. 7. The number of osteocyte canaliculi per osteocyte lacuna (N.Ot.Ca/Ot.Lc) interfacing the (a) porous and (b) solid implants, and the corresponding regions of the native bone. Box-and-whisker plots showing the N.Ot.Ca/Ot.Lc at the (c) porous and (d) solid implant interfaces, and the corresponding regions of the native bone. (e) The average number of osteocytes adjacent to the upper 1/3rd, and the lower 2/3rd of each implant surface and in the native bone (mean values ± SD, # = statistical significance vs. bone, ∗ = statistical significance between the groups indicated by the horizontal bar).

interfacial tissue than the native bone, this band is not entirely specific to collagen, and may represent non-collagenous proteins, as well as poly(methylmethacrylate) (PMMA) in the embedding resin [32].

In areas where osteocytes were not separated from the implant surface by an intervening layer of marrow or osteoid, the osteocytes located up to ∼20 μm from the implant surface demonstrated morphological features of osteocytes found in 'less aged' tissue, i.e., higher average number of osteocyte canaliculi per osteocyte lacuna (N.Ot.Ca/Ot.Lc). In a corresponding manner, EDX elemental analysis showed the Ca/P ratio of the interfacial tissue up to ∼20 μm from the implant surface to be consistently lower

than native bone. The variation in Ca/P ratios partly indicates differences in tissue maturity. The C/Ca ratio reflects the carbon present in the organic matrix and the carbonate ions in bone apatite, and may be particularly high during the early mineralisation stages when the apatite-to-collagen and the collagen-to-matrix ratios may be lower than completely mineralised bone. However, the C/Ca ratio of the native bone, here, may be majorly attributable to the degree of carbonation and to the organic matrix components only to a lesser extent, as demonstrated by the carbonate-to-matrix ratio ($\nu_1\ CO_3^{2-}$/Amide I) being higher for the native bone than the interfacial tissue.

The higher osteocyte density (N.Ot/B.Ar) observed adjacent to the porous implants supports further the hypothesis that topological optimisation of the implant surface, while aimed at inducing rapid early bone formation around the implant, is able to retain a higher proportion of osteocytes in a 'less aged' state with subsequent implications for sensing mechanical loading. A higher osteocyte density adjacent to the EBM surface may possibly be related to the recruitment of osteoprogenitor cells in greater numbers, leading to a higher proportion of osteoblasts becoming embedded within the extracellular matrix to terminally differentiate into osteocytes. One limitation of the present work is that the implants were not subjected to direct functional loading, although mechanical stimulation of the healing sites under normal physical activity cannot be entirely ruled out.

The regions of new-formed bone where osteocytes directly contact the implant surface, assuming contact osteogenesis, are likely to be the earliest formed regions and should therefore exhibit features of relatively mature bone tissue. However, compositional and ultrastructural observations suggest that the interfacial tissue retains a 'less aged' state, and therefore it appears pertinent to inquire whether the 'less aged' state of the interfacial tissue is attributable to a localised, high bone turnover, or because the interfacial region fails to attain complete tissue maturity. Experiments conducted in a canine model suggest that full mineralisation of bone adjacent to hydroxyapatite-coated CoCr implants is not achieved until approximately 18 months of healing [56]. However, it is difficult to estimate to what extent the mineralisation process is influenced or accelerated by the presence of a phosphate-rich hydroxyapatite coating. Moreover, it has been observed in long-term functionally loaded conditions in the human that osteocytes near the implant surface retain a 'less aged' morphology compared to osteocytes located outside the implant thread [45]. Therefore it may be asked whether complete maturation of the interfacial tissue is at all possible without the presence of calcium phosphate rich osteostimulative biomaterials, or even desirable, since it may in fact render the interfacial tissue more fragile and more susceptible to failure under mechanical loading.

The composition (quantitatively) and the N.Ot.Ca/Ot.Lc (qualitatively) of the interfacial tissue adjacent to the EBM surface within the open-pore area (lower 2/3rd) did not appear to be dramatically dissimilar from the interfacial tissue outside (upper 1/3rd), indicating that bone perhaps does not form much differently inside the open-pore area compared to the outside. Importantly, the presence of vasculature within the open-pore areas indicates that the bone formed here retains the capacity for nutrient exchange and the removal of metabolites, and also the possibility for the migration

Table 2
Osteocyte density at the interface and in the native bone.

Location	Total mineralised bone area (μm²)	Mineralised bone area per image (μm²)	Total N.Ot (#)	N.Ot per image (#)	N.Ot/B.Ar (#/mm²)
Porous (upper 1/3rd)	2084648	347441 ± 14031 (n = 6)	2486	414 ± 29	1193 ± 23
Porous (lower 2/3rd)	6530291	544191 ± 243372 (n = 12)	6565	547 ± 222	1005 ± 27
Solid (upper 1/3rd)	2026467	337745 ± 8041 (n = 6)	1950	325 ± 16	962 ± 33
Solid (lower 2/3rd)	4108726	342394 ± 40645 (n = 12)	3883	324 ± 63	945 ± 22
Bone	13891995	578833 ± 176284 (n = 24)	9598	400 ± 105	696 ± 69

of precursor cells responsible for bone resorption and remodelling, as may be expected external to these open-pore areas. Albeit, there was one major difference between the two locations: the N.Ot/B.Ar being considerably higher outside the open-pore area (upper 1/3rd) than the N.Ot/B.Ar within the open-pore area (lower 2/3rd). Whether this is related to differences in the mechanical situation or to differences in the local microenvironment requires further systematic evaluation. Mechanical loading is of key importance for osteocyte survival [57]; and around bone anchored implants, substantial remodelling is said to occur after a period of initial bone formation (e.g., between 1 and 5 years in human) [58]. And with such remodelling a larger number of osteocytes is included in order to provide adequate homeostatic support while the bone tissue undergoes organisation to optimise the capacity for biomechanical loading [58]. Nevertheless, statistically significant differences were observed between the composition as well as the N.Ot/B.Ar of bone formed adjacent to the two implant types, confirming that bone does indeed form differently depending on the surface structure.

With bone being a complex, hierarchically organised, and a highly heterogeneous tissue, it is essential to correlate the composition and structure to be able to understand the functional adaptations of bone, particularly at engineered surfaces of bone, for example the bone-implant interface. Although a commonly employed method, resin infiltration may influence the composition of bone and could be considered a limitation of this work. The proposed methodology to investigate the bone-implant interface allows correlative *in situ* compositional and ultrastructural analysis, beyond merely the detection of calcium ions or phosphate-groups in the tissue.

5. Conclusions

After prolonged healing, the interfacial tissue remained, compositionally, less mature than the native bone, supported by the 'less aged' morphology of the osteocyte lacuno-canalicular network and a significantly higher osteocyte density. Bone healing had progressed further at the EBM surface (porous implants), as evidenced by a higher v_1 CO_3^{2-}/v_2 PO_4^{3-} ratio, and lower Phe and Tyr levels. In the upper 1/3rd regions, the higher N.Ot/B.Ar adjacent to the porous implants indicates a potentially greater capacity for sensing mechanical loading. For the porous implants, the higher N.Ot/B.Ar at the upper 1/3rd vs. the open-pore area suggests 'less aged' tissue, possibly related to differences in the relative rates of remodelling.

Acknowledgements

Appendix A. Supplementary data

Supplementary data associated with this article can be found, in the online version, at http://dx.doi.org/10.1016/j.actbio.2015.11.013.

References

[1] G. Ryan, A. Pandit, D.P. Apatsidis, Fabrication methods of porous metals for use in orthopaedic applications, Biomaterials 27 (2006) 2651–2670.

[2] P. Heinl, L. Müller, C. Körner, R.F. Singer, F.A. Müller, Cellular Ti–6Al–4V structures with interconnected macro porosity for bone implants fabricated by selective electron beam melting, Acta Biomater. 4 (2008) 1536–1544.

[3] P. Thomsen, J. Malmström, L. Emanuelsson, M. Rene, A. Snis, Electron beam-melted, free-form-fabricated titanium alloy implants: material surface characterization and early bone response in rabbits, J. Biomed. Mater. Res. B Appl. Biomater. 90B (2009) 35–44.

[4] A. Palmquist, A. Snis, L. Emanuelsson, M. Browne, P. Thomsen, Long-term biocompatibility and osseointegration of electron beam melted, free-form-fabricated solid and porous titanium alloy: experimental studies in sheep, J. Biomater. Appl. 27 (2013) 1003–1016.

[5] S. Weiner, H.D. Wagner, The material bone: structure-mechanical function relations, Annu. Rev. Mater. Sci. 28 (1998) 271–298.

[6] P. Fratzl, R. Weinkamer, Nature's hierarchical materials, Prog. Mater. Sci. 52 (2007) 1263–1334.

[7] J.S. Yerramshetty, O. Akkus, The associations between mineral crystallinity and the mechanical properties of human cortical bone, Bone 42 (2008) 476–482.

[8] T.A. Franz-Odendaal, B.K. Hall, P.E. Witten, Buried alive: how osteoblasts become osteocytes, Dev. Dyn. 235 (2006) 176–190.

[9] S. Burra, D.P. Nicolella, W.L. Francis, C.J. Freitas, N.J. Mueschke, K. Poole, et al., Dendritic processes of osteocytes are mechanotransducers that induce the opening of hemichannels, Proc. Natl. Acad. Sci. USA 107 (2010) 13648–13653.

[10] L.F. Bonewald, The amazing osteocyte, J. Bone Miner. Res. 26 (2011) 229–238.

[11] M. Kerschnitzki, W. Wagermaier, P. Roschger, J. Seto, R. Shahar, G.N. Duda, et al., The organization of the osteocyte network mirrors the extracellular matrix orientation in bone, J. Struct. Biol. 173 (2011) 303–311.

[12] P. Milovanovic, E.A. Zimmermann, M. Hahn, D. Djonic, K. Püschel, M. Djuric, et al., Osteocytic canalicular networks: morphological implications for altered mechanosensitivity, ACS Nano 7 (2013) 7542–7551.

[13] C.J. Hernandez, R.J. Majeska, M.B. Schaffler, Osteocyte density in woven bone, Bone 35 (2004) 1095–1099.

[14] B. Busse, D. Djonic, P. Milovanovic, M. Hahn, K. Puschel, R.O. Ritchie, et al., Decrease in the osteocyte lacunar density accompanied by hypermineralized lacunar occlusion reveals failure and delay of remodeling in aged human bone, Aging Cell 9 (2010) 1065–1075.

[15] J.D. Currey, K. Brear, P. Zioupos, The effects of ageing and changes in mineral content in degrading the toughness of human femora, J. Biomech. 29 (1996) 257–260.

[16] D.B. Burr, The contribution of the organic matrix to bone's material properties, Bone 31 (2002) 8–11.

[17] B. Busa, L.M. Miller, C.T. Rubin, Y.X. Qin, S. Judex, Rapid establishment of chemical and mechanical properties during lamellar bone formation, Calcified Tissue Int. 77 (2005) 386–394.

[18] B. Wopenka, J.D. Pasteris, A mineralogical perspective on the apatite in bone, Mater. Sci. Eng. C 25 (2005) 131–143.

[19] M.G. Taylor, S.F. Parker, K. Simkiss, P.C.H. Mitchell, Bone mineral: evidence for hydroxy groups by inelastic neutron scattering, Phys. Chem. Chem. Phys. 3 (2001) 1514–1517.

[20] J.D. Pasteris, B. Wopenka, J.J. Freeman, K. Rogers, E. Valsami-Jones, J.A.M. van der Houwen, et al., Lack of OH in nanocrystalline apatite as a function of degree of atomic order: implications for bone and biomaterials, Biomaterials 25 (2004) 229–238.

[21] G.S. Mandair, M.D. Morris, Contributions of Raman spectroscopy to the understanding of bone strength, BoneKEy Rep. 4 (2015).

[22] A. Awonusi, M.D. Morris, M.M. Tecklenburg, Carbonate assignment and calibration in the Raman spectrum of apatite, Calcified Tissue Int. 81 (2007) 46–52.

[23] J.S. Yerramshetty, C. Lind, O. Akkus, The compositional and physicochemical homogeneity of male femoral cortex increases after the sixth decade, Bone 39 (2006) 1236–1243.

[24] Y. Leung, M.A. Walters, N.C. Blumenthal, J.L. Ricci, J.M. Spivak, Determination of the mineral phases and structure of the bone-implant interface using Raman spectroscopy, J. Biomed. Mater. Res. 29 (1995) 591–594.

[25] M.A. Walters, N.C. Blumenthal, Y. Wang, J.L. Ricci, J.M. Spivak, Molecular structure at the bone-implant interface: a vibrational spectroscopic characterization, Calcified Tissue Int. 59 (1996) 368–369.

[26] C.B. Lopes, A.L. Pinheiro, S. Sathaiah, N.S. Da Silva, M.A. Salgado, Infrared laser photobiomodulation (lambda 830 nm) on bone tissue around dental implants: a Raman spectroscopy and scanning electronic microscopy study in rabbits, Photomed. Laser Surg. 25 (2007) 96–101.

[27] A.L. Pinheiro, N.R. Santos, P.C. Oliveira, G.T. Aciole, T.A. Ramos, T.A. Gonzalez, et al., The efficacy of the use of IR laser phototherapy associated to biphasic ceramic graft and guided bone regeneration on surgical fractures treated with miniplates: a Raman spectral study on rabbits, Lasers Med. Sci. 28 (2013) 513–518.

[28] M. Janko, P. Davydovskaya, M. Bauer, A. Zink, R.W. Stark, Anisotropic Raman scattering in collagen bundles, Opt. Lett. 35 (2010) 2765–2767.

[29] K. Donath, G. Breuner, A method for the study of undecalcified bones and teeth with attached soft tissues. The Sage–Schliff (sawing and grinding) technique, J. Oral Pathol. 11 (1982) 318–326.

[30] V. Mazet, C. Carteret, D. Brie, J. Idier, B. Humbert, Background removal from spectra by designing and minimising a non-quadratic cost function, Chemom. Intell. Lab. Syst. 76 (2005) 121–133.

[31] M.D. Morris, G.S. Mandair, Raman assessment of bone quality, Clin. Orthopaedics Related Res. 469 (2011) 2160–2169.

[32] M. Kazanci, H.D. Wagner, N.I. Manjubala, H.S. Gupta, E. Paschalis, P. Roschger, et al., Raman imaging of two orthogonal planes within cortical bone, Bone 41 (2007) 456–461.

[33] A. Roschger, S. Gamsjaeger, B. Hofstetter, A. Masic, S. Blouin, P. Messmer, et al., Relationship between the $\nu(2)PO(4)$/amide III ratio assessed by Raman spectroscopy and the calcium content measured by quantitative backscattered electron microscopy in healthy human osteonal bone, J. Biomed. Opt. 19 (2014) 065002.

[34] S. Gamsjaeger, A. Masic, P. Roschger, M. Kazanci, J.W. Dunlop, K. Klaushofer, et al., Cortical bone composition and orientation as a function of animal and tissue age in mice by Raman spectroscopy, Bone 47 (2010) 392–399.

[35] KA. Dooley, Raman Spectroscopic Studies of Bone Biomechanical Function and Development in Animal Models, University of Michigan, 2011.

[36] M. Kozielski, T. Buchwald, M. Szybowicz, Z. Blaszczak, A. Piotrowski, B. Ciesielczyk, Determination of composition and structure of spongy bone tissue in human head of femur by Raman spectral mapping, J. Mater. Sci. Mater. Med. 22 (2011) 1653–1661.

[37] A.L. Boskey, L. Spevak, R.S. Weinstein, Spectroscopic markers of bone quality in alendronate-treated postmenopausal women, Osteoporos. Int. 20 (2009) 793–800.

[38] H. Isaksson, M.J. Turunen, L. Rieppo, S. Saarakkala, I.S. Tamminen, J. Rieppo, et al., Infrared spectroscopy indicates altered bone turnover and remodeling activity in renal osteodystrophy, J. Bone Miner. Res. 25 (2010) 1360–1366.

[39] G. Falgayrac, S. Facq, G. Leroy, B. Cortet, G. Penel, New method for Raman investigation of the orientation of collagen fibrils and crystallites in the Haversian system of bone, Appl. Spectrosc. 64 (2010) 775–780.

[40] N.J. Crane, W. Wang, J.M.A. Ignelzi, M.D. Morris, Spectral imaging of mouse calvaria undergoing craniosynstosis, Proc. SPIE 4959, Spectral Imaging: Instrumentation, Applications, and Analysis II (2003) 111–119.

[41] G. Penel, G. Leroy, C. Rey, E. Bres, MicroRaman spectral study of the PO_4 and CO_3 vibrational modes in synthetic and biological apatites, Calcified Tissue Int. 63 (1998) 475–481.

[42] M. Janko, A. Zink, A.M. Gigler, W.M. Heckl, R.W. Stark, Nanostructure and mechanics of mummified type I collagen from the 5300-year-old Tyrolean Iceman, Proc. Biol. Sci. 277 (2010) 2301–2309.

[43] C. Gullekson, L. Lucas, K. Hewitt, L. Kreplak, Surface-sensitive Raman spectroscopy of collagen I fibrils, Biophys. J. 100 (2011) 1837–1845.

[44] B.G. Frushour, J.L. Koenig, Raman scattering of collagen, gelatin, and elastin, Biopolymers 14 (1975) 379–391.

[45] F.A. Shah, X. Wang, P. Thomsen, K. Grandfield, A. Palmquist, High-resolution visualization of the osteocyte lacuno-canalicular network juxtaposed to the surface of nanotextured titanium implants in human, ACS Biomater. Sci. Eng. 1 (2015) 305–313.

[46] O. Akkus, F. Adar, M.B. Schaffler, Age-related changes in physicochemical properties of mineral crystals are related to impaired mechanical function of cortical bone, Bone 34 (2004) 443–453.

[47] J.J. Freeman, B. Wopenka, M.J. Silva, J.D. Pasteris, Raman spectroscopic detection of changes in bioapatite in mouse femora as a function of age and in vitro fluoride treatment, Calcif. Tissue Int. 68 (2001) 156–162.

[48] R.Z. Legeros, O.R. Trautz, J.P. Legeros, E. Klein, W.P. Shirra, Apatite crystallites: effects of carbonate on morphology, Science 155 (1967) 1409–1411.

[49] D.E. Steflik, P.J. Hanes, A.L. Sisk, G.R. Parr, M.J. Song, F.T. Lake, et al., Transmission electron microscopic and high voltage electron microscopic observations of the bone and osteocyte activity adjacent to unloaded dental implants placed in dogs, J. Periodontol. 63 (1992) 443–452.

[50] L. Galvis, J.W. Dunlop, G. Duda, P. Fratzl, A. Masic, Polarized Raman anisotropic response of collagen in tendon: towards 3D orientation mapping of collagen in tissues, PloS One 8 (2013) e63518.

[51] A. Bonifacio, V. Sergo, Effects of sample orientation in Raman microspectroscopy of collagen fibers and their impact on the interpretation of the amide III band, Vib. Spectrosc. 53 (2010) 314–317.

[52] M. Bennet, A. Akiva, D. Faivre, G. Malkinson, K. Yaniv, S. Abdelilah-Seyfried, et al., Simultaneous Raman microspectroscopy and fluorescence imaging of bone mineralization in living zebrafish larvae, Biophys. J. 106 (2014) L17–L9.

[53] E.M. McNerny, B. Gong, M.D. Morris, D.H. Kohn, Bone fracture toughness and strength correlate with collagen cross-link maturity in a dose-controlled lathyrism mouse model, J. Bone Miner. Res. 30 (2015) 455–464.

[54] S. Pallu, G.Y. Rochefort, C. Jaffre, M. Refregiers, D.B. Maurel, D. Benaitreau, et al., Synchrotron ultraviolet microspectroscopy on rat cortical bone: involvement of tyrosine and tryptophan in the osteocyte and its environment, PloS One 7 (2012) e43930.

[55] S. Shivtiel, O. Kollet, K. Lapid, A. Schajnovitz, P. Goichberg, A. Kalinkovich, et al., CD45 regulates retention, motility, and numbers of hematopoietic progenitors, and affects osteoclast remodeling of metaphyseal trabecules, J. Exp. Med. 205 (2008) 2381–2395.

[56] S. Döpner, F. Müller, P. Hildebrandt, R.T. Müller, Integration of metallic endoprotheses in dog femur studied by near-infrared Fourier-transform Raman microscopy, Biomaterials 23 (2002) 1337–1345.

[57] A. Bakker, J. Klein-Nulend, E. Burger, Shear stress inhibits while disuse promotes osteocyte apoptosis, Biochem. Biophys. Res. Commun. 320 (2004) 1163–1168.

[58] A. Piattelli, L. Artese, E. Penitente, F. Iaculli, M. Degidi, C. Mangano, et al., Osteocyte density in the peri-implant bone of implants retrieved after different time periods (4 weeks to 27 years), J. Biomed. Mater. Res. B Appl. Biomater. 102 (2014) 239–243.